

Calorimetry at a Future Linear Collider

Steven Green
of Emmanuel College

A dissertation submitted to the University of Cambridge
for the degree of Doctor of Philosophy

Abstract

This thesis describes the optimisation of the calorimeter design for collider experiments at the future Compact Linear Collider (CLIC) and the International Linear Collider (ILC). The detector design of these experiments is built around high-granularity Particle Flow Calorimetry that, in contrast to traditional calorimetry, uses the energy measurements for charged particles from the tracking detectors. This can only be realised if calorimetric energy deposits from charged particles can be separated from those of neutral particles. This is made possible with fine granularity calorimeters and sophisticated pattern recognition software, which is provided by the PandoraPFA algorithm. This thesis presents results on Particle Flow calorimetry performance for a number of detector configurations. To obtain these results a new calibration procedure was developed and applied to the detector simulation and reconstruction to ensure optimal performance was achieved for each detector configuration considered.

This thesis also describes the development of a software compensation technique that vastly improves the intrinsic energy resolution of a Particle Flow Calorimetry detector. This technique is implemented within the PandoraPFA framework and demonstrates the gains that can be made by fully exploiting the information provided by the fine granularity calorimeters envisaged at a future linear collider.

A study of the sensitivity of the CLIC experiment to anomalous gauge couplings that effect vector boson scattering processes is presented. These anomalous couplings provide insight into possible beyond standard model physics. This study, which utilises the excellent jet energy resolution from Particle Flow Calorimetry, was performed at centre-of-mass energies of 1.4 TeV and 3 TeV with integrated lumi-

nosities of 1.5ab^{-1} and 2ab^{-1} respectively. The precision achievable at CLIC is shown to be approximately one to two orders of magnitude better than that currently offered by the LHC.

Finally, a study into various technology options for the CLIC vertex detector is described.

Declaration

This dissertation is the result of my own work, except where explicit reference is made to the work of others, and has not been submitted for another qualification to this or any other university. This dissertation does not exceed the word limit for the respective Degree Committee.

Andy Buckley

Acknowledgements

Of the many people who deserve thanks, some are particularly prominent, such as my supervisor...

Preface

This thesis describes my research on various aspects of the LHCb particle physics program, centred around the LHCb detector and LHC accelerator at CERN in Geneva.

For this example, I'll just mention Chapter ?? and Chapter ??.

Contents

1	Particle Flow Calorimetry for Future Linear Colliders	1
1.1	Particle Flow Calorimetry	1
1.2	International Large Detector	3
1.2.1	Overview	4
1.2.2	Vertex Detector	5
1.2.3	Time Projection Chamber	5
1.2.4	Supplemental Silicon Tracking System	6
1.2.5	Electromagnetic Calorimeter	9
1.2.6	Hadronic Calorimeter	11
1.2.7	Solenoid, Yoke and Muon System	12
1.2.8	Forward Calorimetry	13
1.3	Simulation	15
1.4	CLIC ILD	15
1.4.1	Experimental Conditions at CLIC	17
1.5	Particle Flow Reconstruction	19
1.5.1	PandoraPFA	19
1.5.2	Performance	22
	Bibliography	27
	List of figures	29
	List of tables	31

*“Writing in English is the most ingenious torture
ever devised for sins committed in previous lives.”*

— James Joyce

Chapter 1

Particle Flow Calorimetry for Future Linear Colliders

“I am fond of pigs. Dogs look up to us. Cats look down on us. Pigs treat us as equals.”

— Winston Churchill

Particle flow calorimetry can provide extremely good jet energy resolutions for at a future linear collider. Jet energy resolution is crucial at the linear collider as many of the interesting processes will be characterised by multi-jet final states. Many of these multi-jet final states will be produced from the hadronic decays of W and Z bosons and one of the key goals of the future linear collider is to be able to separate these decays. Separation of these decays can be achieved, however, only by placing a tight requirement on the jet energy resolution; $\sigma_E/E \lesssim 3.5\%$ for 50-500 GeV jets at the ILC and up to 1.5 TeV at CLIC [1]. The use of particle flow calorimetry will also be highly beneficial for quantifying final states of interest that involving charged leptons and missing momentum.

1.1 Particle Flow Calorimetry

The premise of particle flow calorimetry is to use the sub-detector that offers the best energy resolution to measure the energy of any given particle, which corresponds to energy measurements being made in the ECal for γ s, the HCal for neutral hadrons

and, crucially, the tracker for charged particles. The starkest contrast of this approach to that of traditional calorimetry occurs in the measurement of the energy of charged particles. In particle flow calorimetry the energy of a charged particle is measured using the curvature of the path it transverses as it bends in a magnetic field, while in traditional calorimetry the energy would be measured using the calorimeters, predominantly the hadronic calorimeter (HCal). The tracker energy resolution for a single charged particle of energy E_{X^\pm} is $\sim 10^{-4} \times E_{X^\pm}^2$, while for the HCal it is $\sim 0.55 \times \sqrt{E_{X^\pm}}$ [1]. The energy resolution offered by the tracker is significantly better than that offered by the HCal for energies up to $\sim \mathcal{O}(300 \text{ GeV})$. This means that particle flow calorimetry has the potential to offer a much better energy resolution for charged particles, below $\sim \mathcal{O}(300 \text{ GeV})$, than that of the traditional calorimetry approach. Particle flow calorimetry offers gains in performance for collision energies well beyond 300 GeV as the average long-lived particle energy for physics processes of interest is typically much less than 300 GeV. Furthermore, it also leads to a significant improvement in the measurement of jet energies as, after the decay of short-lived particles, approximately 60% of the energy of a jet is carried in the form of charged particles. The measurement of jet energies in the particle flow paradigm is summarised in table 1.1. The benefits to the energy resolution, for both charged particles and jets, offered by the particle flow approach to calorimetry is the driving factor behind why it is planned for use at the linear collider experiment.

Jet Component	Detector	Energy Fraction	Energy Resolution
Charged Particles (X^\pm)	Tracker	$\sim 0.6E_j$	$10^{-4} \times E_{X^\pm}^2$
Photons (γ)	ECal	$\sim 0.3E_j$	$0.15 \times \sqrt{E_\gamma}$
Neutral Hadrons (X^0)	HCal	$\sim 0.1E_j$	$0.55 \times \sqrt{E_{X^0}}$

Table 1.1: The approximate jet fractions and energy resolutions for charged particles (X^\pm) of energy E_{X^\pm} , photons (γ) of energy E_γ and neutral hadrons (X^0) of energy E_{X^0} . Taken from [1].

Particle flow calorimetry is challenging to put into practice as it requires a precise reconstruction for all long-lived particles within a detector. Charged particle energy measurements are made using the curvature of the track they transverse as they bend in the magnetic field, but they also produce calorimetric energy deposits, as shown in figure 1.1. If both energy measurements are included, the energy of the charged particle

will be double counted. To avoid this, any calorimetric energy deposits associated to charged particle tracks must not be used when reporting the reconstructed energy. Furthermore, if the calorimetric energy deposits for a neutral particle are incorrectly associated to a track, the energy measurement for that neutral particle will be totally omitted. The combination of this double counting of charged particle energies and loss of neutral particle energies degrades the energy resolution. This is referred to as the ‘confusion’ contribution to the jet energy resolution. Particle flow calorimetry hinges on the event reconstruction being able to correctly associate all charged particle tracks to their corresponding calorimetric energy deposits. This can only be realised using calorimeters with fine segmentation so that it is possible to resolve individual particle showers. It also required sophisticated pattern recognition algorithms to reduce the effects of confusion.

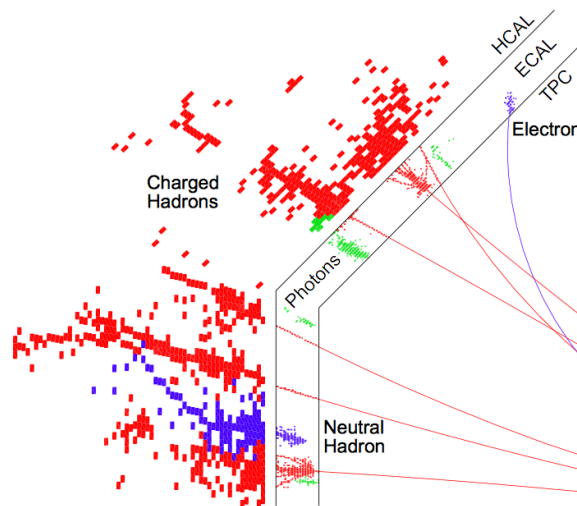


Figure 1.1: A typical simulated 250 GeV jet in the CLIC_ILD detector, with labels identifying constituent particles. Image taken from [2].

1.2 International Large Detector

The current detector concepts for the linear collider experiments have been designed to make particle flow calorimetry possible. While there are a number of different concepts that are under consideration for both the ILC and CLIC one of the most prominent, and the focus of this work, is the International Large Detector (ILD). The ILD detector, shown in figure 1.2, achieves very high spatial resolution for all sub-detector systems thanks to its highly segmented calorimeters and central tracking system, both of which

are encompassed within a 3.5 T magnetic field. The sophisticated pattern recognition software that is needed for particle flow calorimetry is provided by PandoraPFA [1,2].

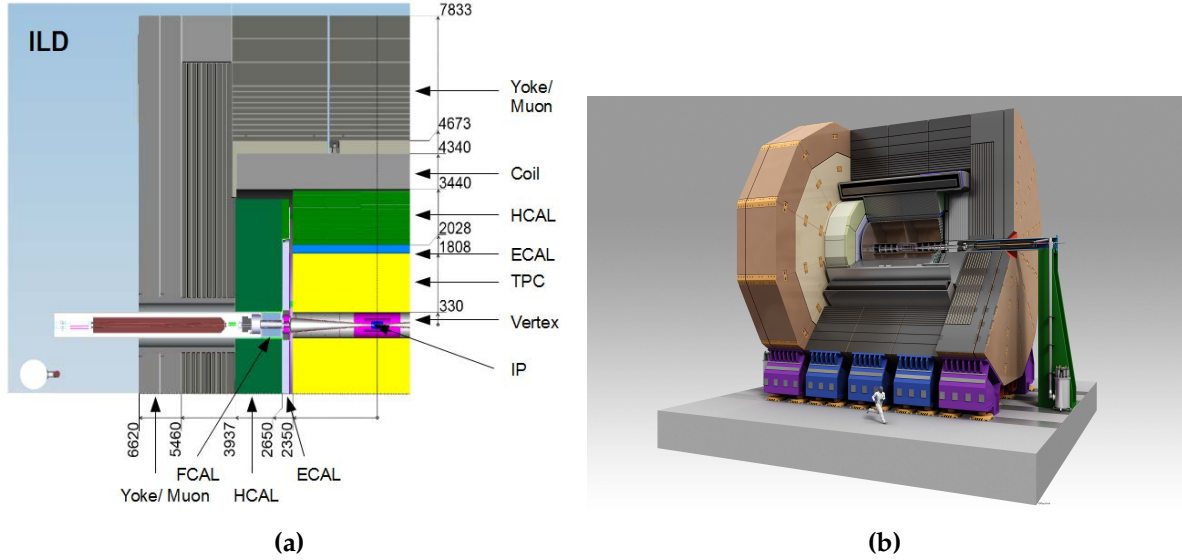


Figure 1.2: (a) Quadrant view of the ILD detector concept. The interaction point is in the lower right corner of the picture. Dimensions are in mm. (b) An artistic view of the ILD detector concept. Figures taken from [3].

1.2.1 Overview

FILL THIS GAP

The tracking system for the ILD detector consists of a multi-layer pixel-vertex detector, which is surrounded by a system of silicon strip and pixel detectors. These are designed to give precise information about displaced vertices with respect to the impact point, which are crucial for the study of short lived particles such as the D or B mesons. Outside of the vertex detector is the central tracker. In ILD this is a Time Projection Chamber (TPC). The TPC samples each charged particle track at many points giving detailed spatial information that can be used to extract the curvature of the track and hence the momentum of the charged particle that transversed it. Finally, a further silicon strip detector surrounds the TPC to give additional, high precision, space points to aid track fitting.

1.2.2 Vertex Detector

The main goal of the ILD vertex detector is to achieve a resolution on the impact parameter of charged particle tracks of:

$$\sigma_b < 5 \oplus \frac{10}{p \sin(\theta)^{3/2}} \mu\text{m}, \quad (1.1)$$

where σ_b is the resolution on the track impact parameter, p is the momentum of the track and θ is the angle between the track and the vertex detector plane. The first term in this parameterisation is the transverse impact parameters resolution and the second is a multiple-scattering term. This makes precisely tagging secondary vertices from charm and bottom mesons possible. Typically these mesons have relatively short proper lifetimes, τ , such that $c\tau \approx \mathcal{O}(300 \mu\text{m})$. To achieve this impact parameter resolution, a spatial resolution of better than $3 \mu\text{m}$ is required near the impact point (IP). Furthermore, a low material budget of less than 0.15 % of a radiation length per layer is required to ensure that few electromagnetic showers are initiated within the vertex detector. A low pixel occupancy is essential for determining the trajectory of individual tracks in the detector. Furthermore, consideration will have to be given to the mechanical structure of the detector, power consumption and cooling.

There are a number of different pixel technology options under consideration for the vertex detector for the ILD detector. This is an active area of ongoing research and development for the linear collider collaboration. The current design of the vertex detector consists of three concentric layers of double-sided ladders with the first layer contains 10 ladders, the second 11 ladders and the third 17 ladders as shown in figure 1.3. Each ladder has two pixel sensors on each side and the ladder thickness is approximately 2 mm. The radii covered by the detector range from 16 mm to 60 mm from the IP.

1.2.3 Time Projection Chamber

The central tracking system for the ILD detector is a TPC, which is shown in figure 1.4. The TPC consists of a cylindrical gas volume with a central electrode providing an axial electric field. When a charged particle passes through the TPC, it ionises the gas and the ionised molecules drift in the axial electric field. The direction of the electric field is chosen such that the electrons drift towards the endplates where they are collected.

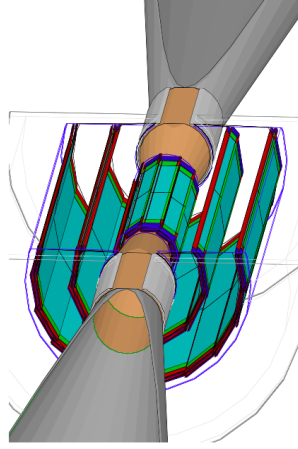


Figure 1.3: Vertex detector design for ILD. Figures taken from [4].

The position of the ionisation point can then be calculated using the drift time of the electrons in the TPC. Combining these TPC hits together makes reconstruction of the full charged particle track possible. TPCs have an advantage over silicon tracking in that they continuously track any charged particle passing through them, while silicon detectors are only sensitive within each silicon layer. This compensates for the worse single point resolution that TPCs have in comparison to silicon detectors and makes TPCs a viable option for the ILD detector. Furthermore, TPCs have a very low material budget. This benefits calorimetry as it minimises energy losses prior to the particle energy entering the calorimeters, which means the calorimetric energy deposits give a better reflection of the true particle energy.

The ILD TPC has a point resolution of better than $100 \mu\text{m}$ and a double hit resolution in ϕ of less than 2 mm . The gas used for the TPC will be $\text{Ar}:\text{CH}_4:\text{CO}_2$ (95:3:2) [5]. Several readout technology options, designed to measure the ionisation current, are currently under development. For all potential options it is envisaged that the readout pads would be $\approx 1 \times 6 \text{ mm}^2$ giving a total of approximately 10^6 pads on each TPC endplate.

1.2.4 Supplemental Silicon Tracking System

There are four components that make up the supplemental silicon tracking system in ILD, shown in figure 1.5, which are:

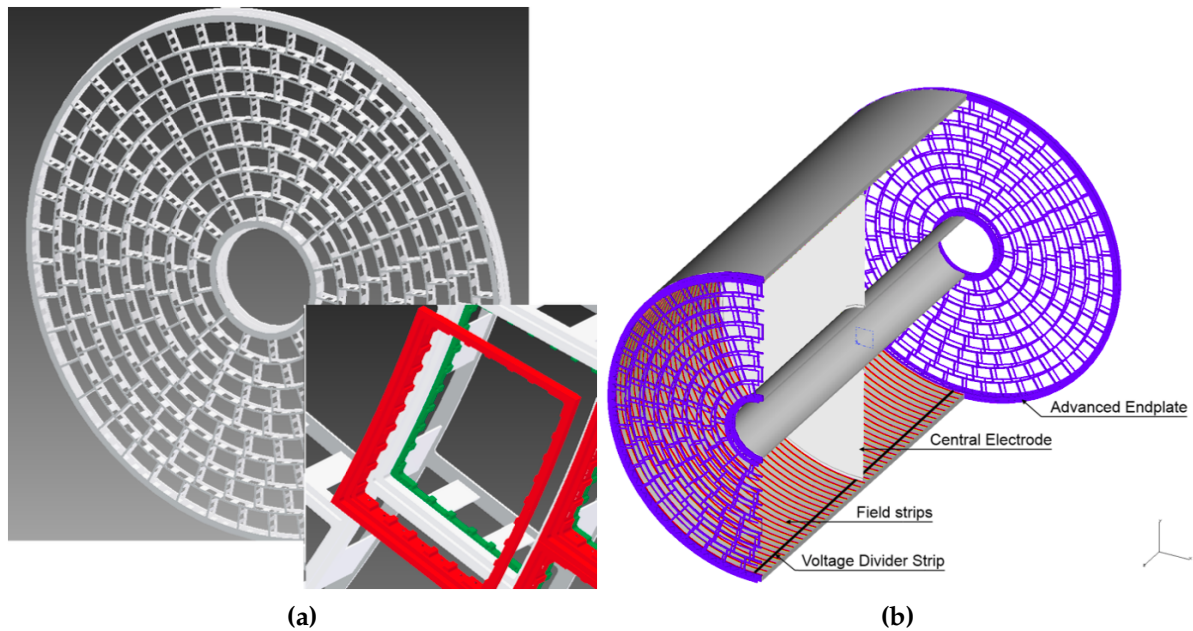


Figure 1.4: (a) Drawing of the proposed end-plate for the TPC. In the insert a back frame, which is designed to support the readout modules, is shown. (b) Conceptual sketch of the TPC system showing the main parts of the TPC (not to scale). The central electrode generates the axial electric field, the endplates collect the ionisation electrons, the field strips help to maintain a uniform electric field across the TPC and the voltage divider strips maintains the voltage difference between the anode and cathode. The field strips are held at fixed voltages such that they replicate the electric field produced by the electrodes. This reinforcing of the electric field configuration minimises non-uniformities in the electric field. The field cage of the TPC is not shown.

- Silicon Inner Tracker (SIT) and Silicon External Tracker (SET). These are both barrel components, which are positioned immediately inside and outside the TPC. The SIT helps form associations between hits in the vertex detector and TPC, while the SET helps with extrapolation of TPC tracks into the calorimeter.
- Endplate of the TPC (ETD). This sensor is identical to the SET, but is positioned in front of the ECal endcap calorimeter. The ETD extends the coverage of the supplemental silicon tracking system envelope.
- Forward tracker (FTD). This detector consists of seven silicon disks that extend the coverage of the tracking down to small angles that are not covered by the TPC.

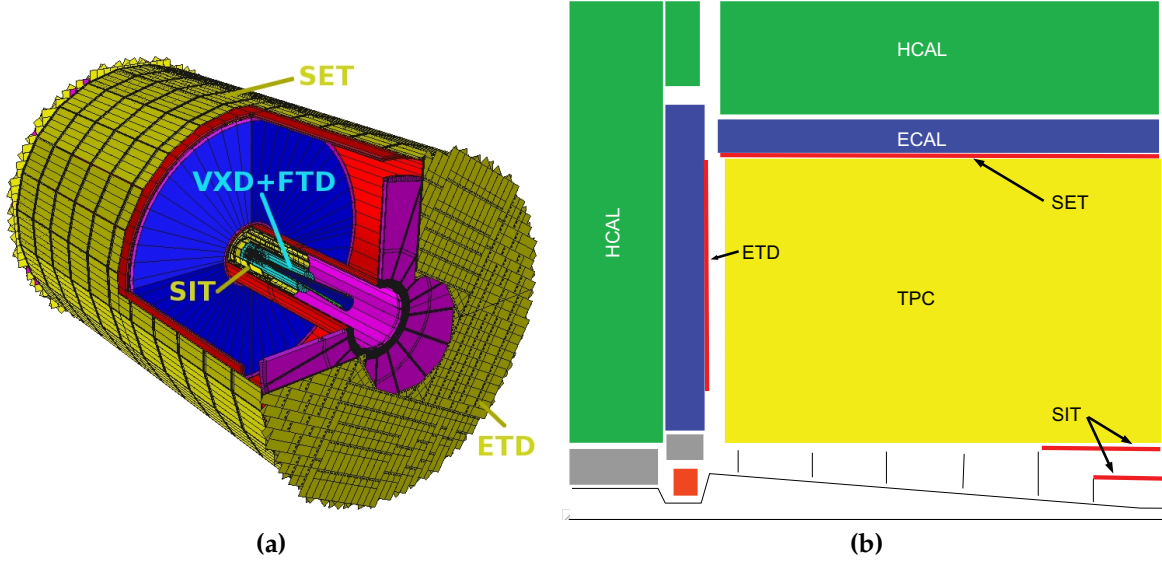


Figure 1.5: (a) A 3D detailed GEANT4 simulation description of the silicon system. (b) A quadrant view of the ILD silicon envelope made of the four components SIT, SET, ETD and FTD as included in the full MOKKA simulation. Figures taken from [3].

Tracking System	Coverage [$\cos\theta$]
SIT	0.910
SET	0.789
ETD	0.799 - 0.985
FTD	0.802 - 0.996

Table 1.2: Coverage of the supplementary silicon tracking systems in the ILD detector. In this table θ is the polar angle with respect to the beam direction. Taken from [3].

The coverage of the SIT, SET, ETD and FTD is given in table 1.2. These detectors are designed to give high precision space points that can be used in track fitting. Furthermore, the ETD and SET are of particular use for extrapolating the charged particle tracks into the calorimeters. This is key for particle flow calorimetry, which relies upon correct association of charged particle tracks and clusters of calorimeter hits. Analogously to the vertex detector, these detectors require low material budget and low occupancy. The FTD, due to its proximity to the beam axis, is particularly prone to high occupancies.

The SIT, SET and ETD are silicon pixel sensors with $50\ \mu\text{m}$ pitch embedded in $200\ \mu\text{m}$ thick silicon. The FTD consists of seven silicon tracking disks, the first two being pixel detectors and the remaining five being strip detectors. The pixel detector

disks are formed of 16 petals, as shown in figure 1.6. Within these petals the pixel size varies from $26 \times 29 \mu\text{m}^2$ to $26 \times 67 \mu\text{m}^2$. Strip detectors are used for the outermost tracking disks as the occupancy considerations do not demand a high granularity detector i.e. a pixel detector. These detector disks will have a pitch of $50 \mu\text{m}$. The active sensor and readout ASIC design for each of these detectors is an active area of development for the linear collider.

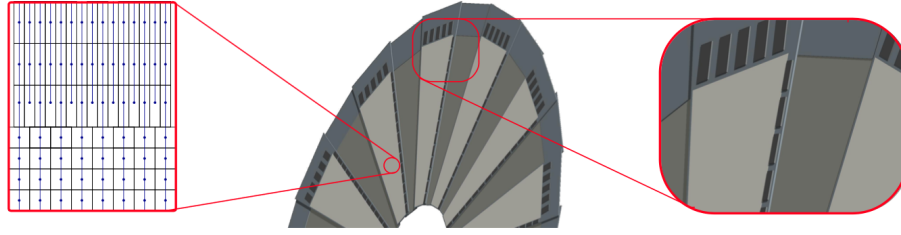


Figure 1.6: A half-disk for the FTD showing the petal concept. The rightmost zoom image showers a detail of the end-of-petal area that houses the read-out electronics. The leftmost image shows the region at $R = 8 \text{ cm}$ where both the column width and the R -dimension of the pixels changes. Figures taken from [3].

1.2.5 Electromagnetic Calorimeter

The nominal ILD detector contains a finely segmented electromagnetic sampling calorimeter (ECal). The ECal surrounds the tracking system in the ILD detector. It has been specifically designed with particle flow calorimetry in mind. To that extent the spatial resolution of particle showers within the ECal takes as much, if not more, precedence than the energy resolution. The primary goal of the ECal is to induce electromagnetic particles to shower within it and to record the energy deposited by those showers.

There are a number of design requirements for the ECal:

- The ECal must be compact in size to reduce the overall cost of the detector.
- Fine segmentation of the ECal is required so that nearby particle showers can be separated. This is an essential requirement for particle flow calorimetry.
- Electromagnetic showers should be contained within the ECal.

Based on these requirements tungsten is used as the absorber material for the ILD ECal as it has a small radiation length (X_0), a small Molière radius and a large ratio

of radiation length to nuclear interaction length. A comparison of these properties for other ECal absorber material candidates is shown in table 1.3. The small radiation length in tungsten allows for a large number of radiation lengths, $\approx 24X_0$, to be compacted within a relatively short distance, ≈ 20 cm, in nominal ILD ECal. This is sufficient for containing all but the highest energy electromagnetic showers. The small Molière radius in tungsten will lead to compact electromagnetic showers. This makes separation of nearby showers easier. Finally, the large ratio of the radiation length to the nuclear interaction length in tungsten will lead to greater longitudinal separation between electromagnetic and hadronic showers again making shower identification easier.

The active material in the nominal ILD ECal is silicon, however, a scintillator strip option is also being considered. It contains a total of 30 readout layers, which is sufficient to provide a good energy resolution. The tungsten thickness for the innermost 20 layers is 2.1 mm, while for the final 10 layers it is 4.2 mm. This configuration of absorber material thickness is chosen to reduce the number of readout channels and hence the cost, while maintaining a high sampling rate for particle showers at the start of the ECal. It should be noted that this ECal offers no gains in terms of energy resolutions in comparison to preexisting particle collider experiments, as shown in table 1.4. This is the case as the focus of this calorimeter is split between imaging the particle showers and recording their energy as opposed to purely focusing on the energy measurement. Each of the ECal layers is divided up into square cells, of side length 5 mm, which makes separation of nearby particle showers possible. This cell size was chosen as a balance between being able to resolve nearby particle showers and reducing the overall cost of the calorimeter, which scales with the number of readout channels. An optimisation study of the various ECal parameters for the ILD detector can be found in section ??.

Material	λ_I (cm)	X_0 (cm)	ρ_M (cm)	$\frac{\lambda_I}{X_0}$
Fe	16.8	1.76	1.69	9.5
Cu	15.1	1.43	1.52	10.6
W	9.6	0.35	0.93	27.4
Pb	17.1	0.56	1.00	30.5

Table 1.3: Comparison of the nuclear interaction length λ_I , radiation length X_0 and Molière radius for iron, copper, tungsten and lead. Table taken from [1].

Experiment	ECal Energy Resolution $\frac{\sigma_E}{E}$
CMS [6]	$\sim \frac{2.8\%}{\sqrt{E(\text{GeV})}} \oplus 0.3\% \oplus \frac{12\%}{E(\text{GeV})}$
ATLAS [7]	$\sim \frac{10.1\%}{\sqrt{E(\text{GeV})}} \oplus 0.1\%$
LHCb [8]	$\sim \frac{9\%}{\sqrt{E(\text{GeV})}} \oplus 0.8\%$
ILC (ILD Silicon Option) [3]	$\sim \frac{16.6\%}{\sqrt{E(\text{GeV})}} \oplus 1.1\%$

Table 1.4: Comparison of the ECal energy resolutions for various experiments.

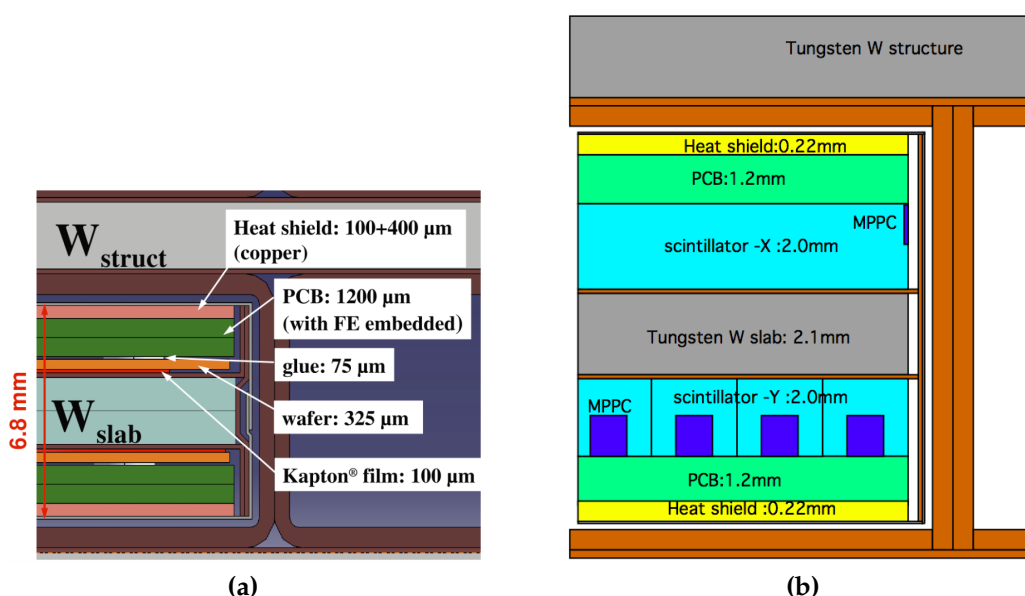


Figure 1.7: Cross section through ECal layer for (a) silicon and (b) scintillator option. Figures taken from [3].

1.2.6 Hadronic Calorimeter

A finely segmented hadronic sampling calorimeter (HCal) is also present in the nominal ILD HCal. This calorimeter surrounds the ECal and, analogously to the ECal, has been designed with particle flow calorimetry in mind. The primary goal of the HCal is to induce hadronic showers within it and record the energy deposited by those showers.

The design requirements for the HCal mirror those of the ECal, which can be found in section 1.2.5, with one exception; the HCal is designed to contain hadronic showers as opposed to electromagnetic showers. Steel is used as the absorber material for the

HCal as it has durable mechanical properties that allow the HCal to be constructed without the need of auxiliary supports. If required, auxiliary supports would create dead regions in the detector that would harm performance. Furthermore, steel is relatively inexpensive and has a relatively small nuclear interaction length, meaning it is possible to achieve a compact calorimeter design at low cost. The nominal ILD HCal contains approximately $6\lambda_I$, which when combined with the $1\lambda_I$ in the ECal is enough to contain the majority of hadronic showers at ILC like energies.

The active material in the nominal ILD HCal is scintillator. In total, the HCal contains 48 readout layers, which provides an extremely good energy resolution. This can be seen when comparing the HCal energy resolution between different experiments, as shown in table 1.5. An individual layer in the HCal is comprised of 20 mm of steel absorber material with 3 mm of scintillator active material. Each layer in the HCal is segmented into square cells, of side length 30 mm. This cell size was chosen as a balance between reducing the cost of the detector, which is proportional to the number of readout channels, and achieving the required spatial resolution to make particle flow calorimetry possible. The segmentation of the ILD HCal gives excellent spatial resolution and sufficiently good energy resolution to make the use of particle flow calorimetry a reality. An optimisation study of the various HCal parameters for the ILD detector can be found in section ??.

Experiment	HCal Energy Resolution $\frac{\sigma_E}{E}$
CMS [9]	$\sim \frac{90\%}{\sqrt{E(\text{GeV})}} \oplus 4.8\%$
ATLAS [10]	$\sim \frac{52.1\%}{\sqrt{E(\text{GeV})}} \oplus 3.0\% \oplus \frac{1.6\%}{E(\text{GeV})}$
LHCb [8]	$\sim \frac{69\%}{\sqrt{E(\text{GeV})}} \oplus 9.0\%$
ILC (ILD Silicon Option) [3]	$\sim \frac{43.3\%}{\sqrt{E(\text{GeV})}} \oplus 1.8\%$

Table 1.5: Comparison of the HCal energy resolutions for various experiments.

1.2.7 Solenoid, Yoke and Muon System

Surrounding the HCal in ILD is a solenoid, which generates a 3.5 T magnetic field. The magnetic field produced by the coil is crucial for bending charged particles so that their momentum can be determined from the curvature of the path they

transverse. Furthermore, the bending of charged particles leads to greater separation of calorimetric energy deposits between charged and neutral particles, which will reduce the effects of confusion when using particle flow calorimetry.

The magnetic field in the ILD detector is returned by an iron yoke that surrounds the solenoid. Iron is chosen for the yoke material as it has a very large permeability.

This yoke is instrumented by a muon system in the barrel and forward regions of the detector. The goal of this instrumentation is to identify muons escaping the calorimeters and to act as a tail catcher for the calorimeters. The muon system consists of 10 layers, spaced 140 mm apart, followed by 2 (3) layers spaced 600 mm apart in the barrel (endcap) region of the detector, as shown in figure 1.8. There is also an additional sensitive layer for the barrel region placed immediately outside the HCal to help with association energy deposits between the calorimeters and the yoke. As the majority of particles at ILC like energies will be contained within the calorimeters, the energy and spatial resolution of the muon system are not critical to performance. It is for that reason that the number of layers is lower and the layer thicknesses wider in the yoke than in the calorimeters. The nominal ILD model uses 30 mm wide and 1 m long scintillator strips as the readout technology for the yoke.

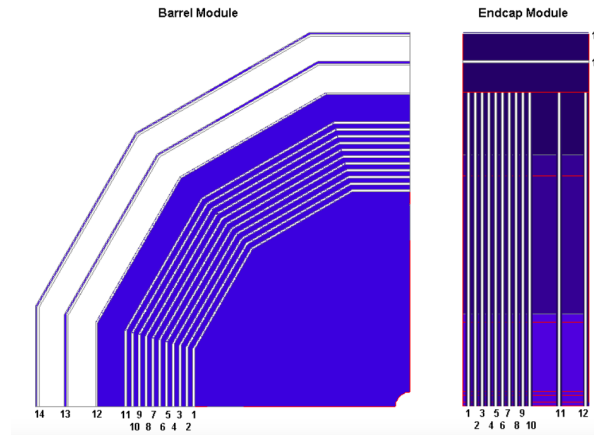


Figure 1.8: The sensitive layers of the ILD muon system. Figure taken from [3].

1.2.8 Forward Calorimetry

Three additional sampling calorimeters are envisaged for the linear collider experiment: the LumiCal, the LHCAL and the BeamCal. Their purpose is to extend the coverage of the detector towards 4π and monitor the beam quality. The LumiCal will

aim to measure the luminosity with a precision of less than 10^{-3} at 500 GeV using Bhabha scattering, $e^+e^- \rightarrow e^+e^-(\gamma)$, as a gauge process [5]. The BeamCal will make a bunch-bunch estimate of the luminosity and assist in the beam tuning. Alongside the LumiCal is the LHCAL, which extends the coverage of the HCal to low polar angle as shown in figure 1.9. The LumiCal covers polar angles between 31 and 77 mrad, while the BeamCal covers the range between 5 and 40 mrad. The presence of beam-induced backgrounds along the beam line means these calorimeters will have to be radiation hard.

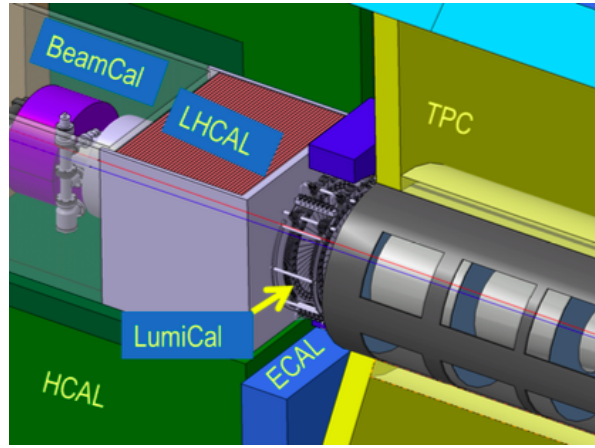


Figure 1.9: The very forward region of the ILD detector. LumiCal, BeamCal and LHCAL are carried by the support tube for the final focusing quadrupole, QD0, and the beam pipe. Figure taken from [3].

As the primary focus of these calorimeters is measuring the e^+e^- beam, they are all constructed using tungsten absorber material to ensure narrow electromagnetic showers form within them. The LumiCal layer configuration mirrors that of the ECAL giving it a total of $\approx 24X_0$ across its 30 layers. Silicon is used as sensitive detector element for the LumiCal. The LHCAL uses silicon readout sensors identical to those found in the LumiCal and in total the LHCAL contains $4\lambda_I$ across 40 layers. The BeamCal sensitive detector material is currently being developed as, due to the high occupancy from the beam induced backgrounds, a fast readout is required. The cell sizes for these calorimeters is yet to be confirmed.

These calorimeters play a minimal role in event reconstruction as few particles from the hard physics interaction will have their energy measured by these calorimeters. It is for this reason that they are not used in the simulation.

1.3 Simulation

In the simulation of the vertex detector silicon is used as the sensitive material. Support material and a cryostat are also included in the simulation for further realism.

In the detector model simulations all of these elements are included with additional material added to represent the support structure.

In the detector simulation the TPC is simulated as a cylindrical volume of the gas mixture surrounded by a field cage. A conservative estimate of the endplate is included in the simulation to account for the support structure, electronics and cooling pipes for the TPC. Furthermore, the material budget required to account for power and readout cables for the inner vertex detector has been estimated and is included in the simulation as an aluminium cylinder between the beam pipe and the field cage of the TPC.

As well as including the silicon tungsten sampling calorimeter, the simulation of the ILD ECal contains additional material to represent the instrumented region of the sensor and a heat shield as shown in figure 1.7.

Simulation of the ILD HCal have a number of realistic features included such as detailed modelling of the electronics, detector gaps and the implementation of Birk's law for the scintillator sensitive detector elements.

In the simulation of the ILD yoke a square cell size of 30 mm is assumed. This is in contrast to the nominal ILD model, but as the tail-catcher plays a minimal role in event reconstruction at ILC like energies this difference should have negligible impact.

1.4 CLIC ILD

The increased collision energy found at the CLIC experiment mean the use of the nominal ILD detector model would be inappropriate. Therefore, a new detector model, CLIC_ILD [11], based upon the nominal ILD detector model was created to cope with the experimental conditions found at the CLIC experiment. Several modifications were made to the nominal ILD detector model to make it more suitable for the CLIC experiment. The key differences between the nominal ILD detector and CLIC_ILD are:

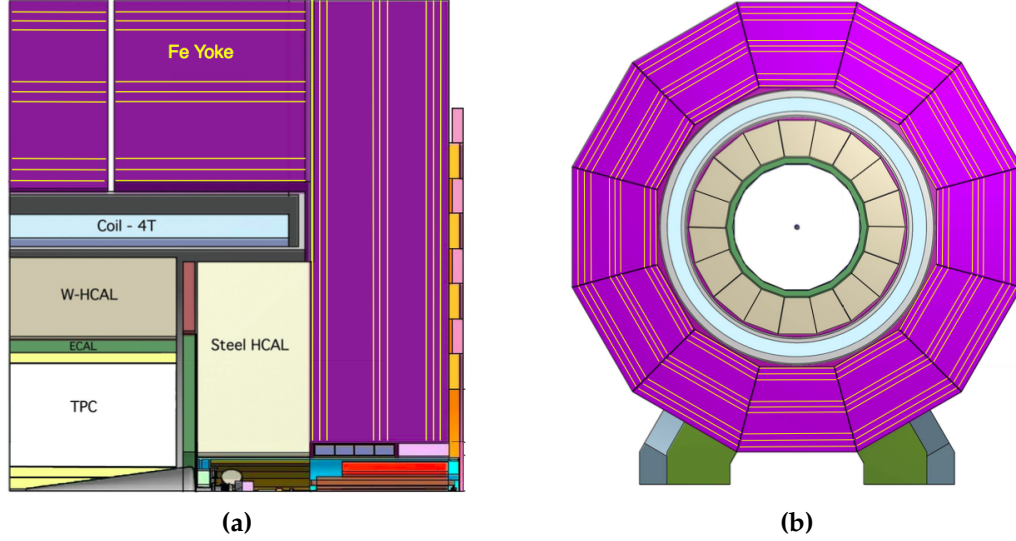


Figure 1.10: (a) Longitudinal (top quadrant) and (b) transverse cross section of the CLIC_ILD detector. Figures taken from [11].

- The higher energies found at the CLIC experiment lead to more intense beam induced backgrounds, which is especially problematic for detectors close to the IP where the occupancies will be extremely high. To attempt to compensate for these effects the inner vertex detector in CLIC_ILD is moved 15 mm further out from the IP.
- The HCal thickness is increased from $6 \lambda_I$ to $7.5 \lambda_I$. This ensures that higher energy particle showers found at the CLIC experiment are in general contained within the calorimeters.
- The HCal absorber material for the barrel is tungsten as opposed to steel. This reduces the overall thickness of the HCal and keeps the coil size, one of the driving cost factors for the detectors, similar for the nominal ILD and CLIC_ILD detectors. In the endcaps steel is used as the absorber material as there are no spatial requirements relating to the coil size and this will lower the detector cost. Furthermore, the shower development time in steel is faster than in tungsten making effective time stamping of energy deposits easier, which is crucial for the CLIC experiment for vetoing beam induced backgrounds.
- The magnetic field strength in the CLIC_ILD detector is increased to 4 T. This was found to benefit the reconstruction, particularly at high energies, as it leads

to greater separation of charged particle tracks. Furthermore, it was possible to achieve this increase in field strength using the nominal ILD coil design.

1.4.1 Experimental Conditions at CLIC

The CLIC experiment will operate in a unique environment in comparison to previous generations of lepton colliders and this must be properly accounted for to get an accurate measure of the physics potential that CLIC has to offer. The following aspects of the CLIC experiment present the largest challenges to the physics potential for the CLIC experiment:

- The high bunch charge density. The small beam size at the impact point produces very large electromagnetic fields. These fields can interact with the opposite beam particles causing them to radiate photons in an effect known as beamstrahlung. Beamstrahlung acts to reduce the collision energy of the e^+e^- pairs.
- Beam related backgrounds. Beamstrahlung photons can subsequently interact to produce background events that must be accounted for. Dominant backgrounds of this form that cannot be easily vetoed in the reconstruction include incoherent pair production of e^+e^- and $\gamma\gamma \rightarrow \text{Hadron}$.
- Fast readout technology is crucial. The CLIC bunch train consists of 312 bunches with a repetition rate of 50 Hz. Each bunch is separated by 0.5ns, therefore, it will be necessary to integrate over multiple bunch crossing when reading out the detectors. This places tight constraints on all detector electrical readout speeds and time resolutions.

Beam-Related Backgrounds at CLIC

The primary sources of background for the CLIC experiment are as follows:

- e^+e^- pair creation from the interaction of a beamstrahlung photons with the opposing beam. The different mechanisms for pair creation are as follows:
 - **Coherent pair production.** This mechanism involves the interaction of a real beamstrahlung photon with the electromagnetic field from the opposing beam.

- **Trident pair production.** This mechanism involves the interaction of a virtual beamstrahlung photon with the electromagnetic field from the opposing beam.
- **Incoherent pair production.** This mechanism involves the interaction of a real or virtual beamstrahlung photon with the individual particles in the opposing beam.
- $\gamma\gamma \rightarrow \text{Hadron}$ from the interaction of real or virtual beamstrahlung photons with each other. Example Feynman diagrams for such processes is shown in figure ??.
- Beam halo muons that arise from interactions of the beam particles during collimation. The dominant mechanisms producing beam halo muons are photon conversions into muon pairs ($\gamma e^- \rightarrow \mu^+ \mu^- e^-$) and annihilation of positrons with atomic e^- into muon pairs ($e^+ e^- \rightarrow \mu^+ \mu^-$) [12].

Each of these has to be properly addressed to get a true measure of the physics potential at CLIC. Coherent and trident pair production is not a dominant source of background as they are produced at low transverse momenta, as figure 1.11 shows, and a simple cut would veto these backgrounds. This is not the case for incoherent pair production of $e^+ e^-$, which are dominant in the forward regions of the detector, and $\gamma\gamma \rightarrow \text{Hadron}$, which are dominant in the tracker and the calorimeters (with the exception of low radii in the calorimeter endcaps) [11, 13]. Beam halo muons are not a major source of background either as they can be easily removed during the reconstruction due to the clear signal they create in the detector. An algorithm was developed within the PandoraPFA framework for this purpose and it was found to be highly effective at removing the beam halo muons background [11].

$\gamma\gamma \rightarrow \text{Hadron}$ events are the most dominant source of background to consider at CLIC as these events deposit more energy throughout the detector than incoherent pair production of $e^+ e^-$ events [11]. The effect of the $\gamma\gamma \rightarrow \text{Hadron}$ background is incorporated into this analysis by overlaying $\gamma\gamma \rightarrow \text{Hadron}$ events onto the event samples used in this analysis. The overlaid backgrounds are added prior to reconstruction so that their effect on the reconstruction is fully accounted for. For a given event the exact number of background events overlaid is drawn from a Poisson distribution with a mean of 3.2 (1.3) events per bunch crossing at 3 (1.4) TeV. While incoherent pairs are still a source of background they will produce a second order effect in comparison to the $\gamma\gamma \rightarrow \text{Hadron}$ events.

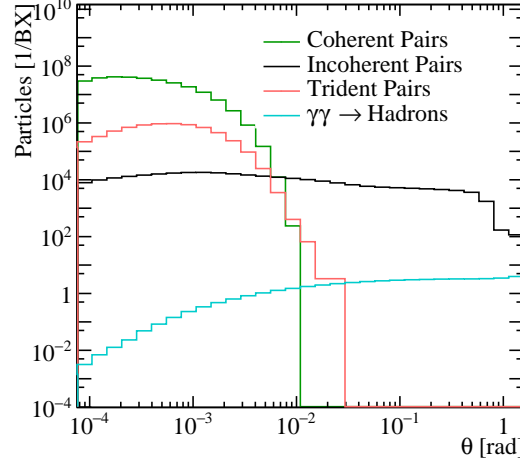


Figure 1.11: Angular distribution of number of particles for beam induced backgrounds for CLIC at $\sqrt{s} = 3$ TeV. Taken from CLIC CDR.

The PFO choices described in section ?? are applied to veto the effect of PFOs that arise from the overlaid $\gamma\gamma \rightarrow \text{Hadron}$ events.

1.5 Particle Flow Reconstruction

Particle flow calorimetry relies upon correct associations being made between calorimetric energy deposits and charged particle tracks. Even with a finely segmented detector, such as the ILD detector described in section 1.2, correctly making these associations is a highly non-trivial task and must be done using advanced pattern recognition software. This is provided by the PandoraPFA particle flow algorithm [1,2].

1.5.1 PandoraPFA

PandoraPFA applies the pattern recognition logic in eight main stages:

1. Track selection. The input track collections are examined to determine whether V^0 decays, two charged tracks originating from a point displaced from the IP, or kinks, where a charged particle has decayed into a single charged particle and a number of neutral ones, are present. Such information will be propagated in the reconstruction to the final PFO creation stage.

2. Calorimeter hit selection. This stage is broken down into several steps:

- The various collection of, post digitisation, calorimeter hits are passed into the Pandora framework and converted into Pandora calorimeter hits. These objects are self describing so that the Pandora pattern recognition logic has no dependancy on the external software framework.
- A minimum ionising particle equivalent energy cut is applied to the calorimeter hits. If a calorimeter hit contains less than 0.5 (0.3) of the energy of a normally incident MIP passing through the calorimeter cell in the ECal (HCal) then it is not used in the reconstruction.
- Calibration of the energy contained within the calorimeter hits is flagged up at this point, however, it is not directly applied at this stage. The energy contribution for each calorimeter cell ultimately depends on whether the associated cluster of calorimeter hits is deemed to originate from an electromagnetic or hadronic shower. Different scale factors are applied to the energy for electromagnetic and hadronic showers to account for effects such as the invisible energy component in hadronic showers. These energy factors are used throughout the reconstruction, including the final reconstructed particle energy, once the particle shower type has been identified. For energy comparisons prior to the shower type being identified the uncorrected calorimeter hit energy is used. Further details on how these calibration constants are determined can be found in section ??.
- To minimise any dependancy on the detector geometry each calorimeter hit is assigned to a pseudo-layer, which is representative of the calorimeter stave layer. All further topological association algorithms work using the pseudo-layer definition, illustrated in figure 1.12.
- If a calorimeter hit is sufficiently far away from other hits, it is flagged as an isolated hit. Such hits are most likely due to low energy neutrons produced in hadronic showers, which can travel a significant distance from the original shower before depositing energy. Due to the distance they travel these hits are very difficult to associate to the correct particle shower. Furthermore, as such hits are unlikely to be the seed for a particle shower they are not used by the initial clustering algorithm.

- Any calorimeter hit that contains an energy consistent with a MIP signal and where, at most, one Pandora calorimeter hit exists in the neighbouring cells within the same layer is flagged as a MIP consistent hit. This information is used in the identification of MIPs in the reconstruction.
3. Clustering. This begins by using the projection of the charged particle tracks onto the front face of the ECal as seeds for the initial clustering phase. Calorimeter hits are looped over on a per layer basis, working from the inner to the outer pseudo-layer, and if they fall within a cone of fixed dimensions surrounding a cluster direction they are associated to the cluster. If no association can be made to any preexisting calorimeter hit clusters then the calorimeter hit is used to seed a new cluster.
 4. Topological cluster merging. The initial clustering algorithm is designed to be conservative to avoid mixing together energy deposits from several particles. The fragments produced by the initial clustering are then merged together by various algorithms whose logic is motivated by a number of well-motivated topological rules, such as those shown figure 1.13.
 5. Statistical re-clustering. Comparisons between the cluster energy and any associated track momenta are made to determine whether they are consistent. If a large discrepancy is observed then statistical re-clustering is initiated. This involves running a number of differently configured algorithms to change the cluster configuration to determine if a new optimal configuration of tracks and clusters can be found.
 6. Photon identification and recovery. Topological likelihood data is used to identify clusters of calorimeter hits that are consistent with γ s. This is possible due to the clear transverse and longitudinal profiles observed for electromagnetic showers.
 7. Fragment removal. Neutral clusters originating from a nearby charged particle cluster are identified and merged back into the parent charged particle cluster. These algorithms take into account the changes in the compatibility of the track and cluster associations when merging any neutral clusters into charged clusters.
 8. Formation of particle flow objects. Finally, reconstructed particles are produced. The energy for charged particles is taken from the track momenta, while neutral particle energies are taken from the calorimeter cluster measurements. Furthermore, the different electromagnetic and hadronic scales are applied to the output

neutral particle energies depending on whether the neutral cluster is consistent with a γ .

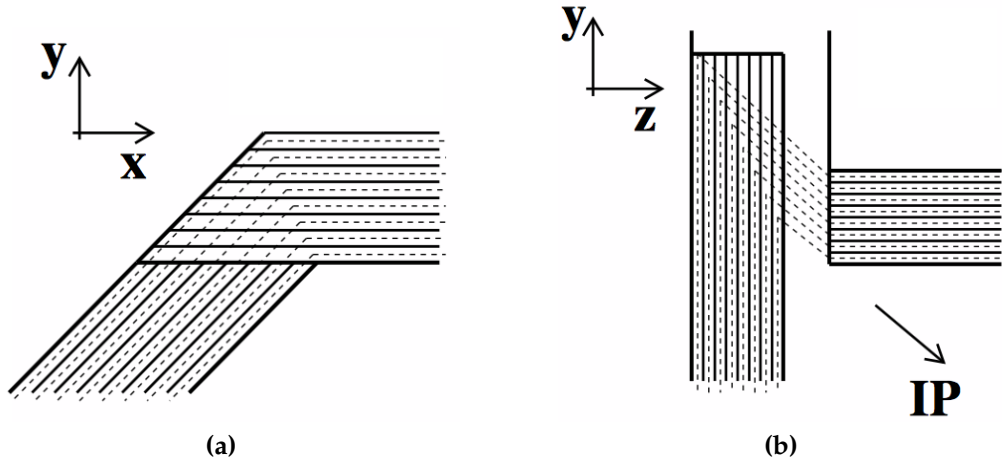


Figure 1.12: Schematic showing the definition of the pseudo-layer assignment for calorimeter hits. The solid lines indicate the positions of the physics ECal layers and the dashed lines show the definition of the virtual pseudo-layers. (a) The xy -view showing the ILD ECal stave structure. (b) The xz view showing a possible layout for the ECal barrel/endcap overlap region. The pseudo-layers are defined using projection back to the IP. Figures taken from [1].

The application of the pattern recognition algorithms in PandoraPFA when combined with a highly segmented detector make particle flow calorimetry a reality. In turn this provides excellent jet energy resolution for studying many interesting physics processes at the linear collider experiment.

1.5.2 Performance

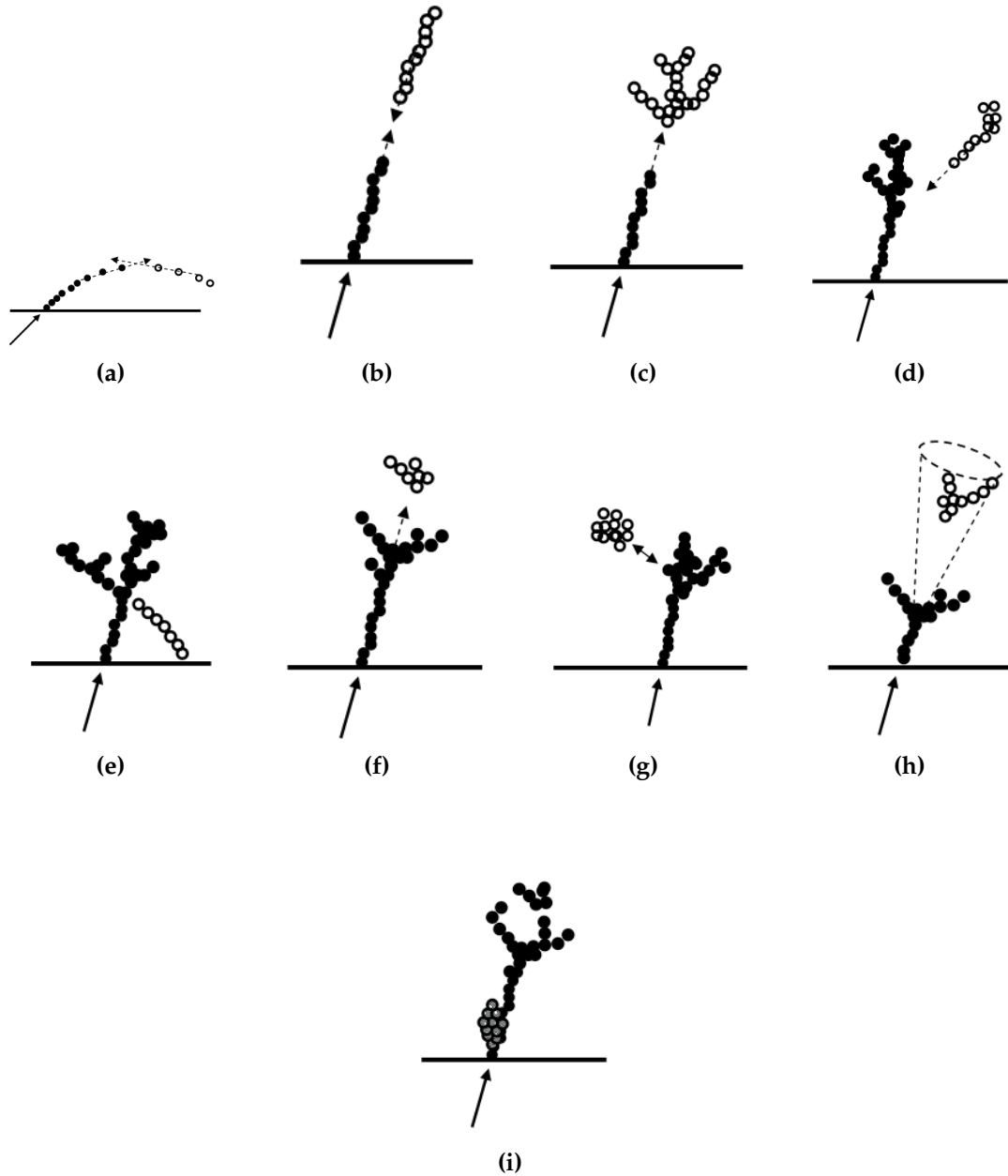


Figure 1.13: The main topological rules for cluster merging: (a) looping track segments; (b) track segments with gaps; (c) track segments pointing to hadronic showers; (d) track-like neutral clusters pointing back to a hadronic shower; (e) back-scattered tracks from hadronic showers; (f) neutral clusters which are close to a charged cluster; (g) a neutral cluster near a charged cluster; (h) cone association; and (i) recover of photons which overlap with a track segment. In each case the arrow indicates the track, the filled points represent the hits in the associated cluster and the open points represent hits in the neutral cluster. Figures taken from [1].

Colophon

This thesis was made in $\text{\LaTeX}2_\epsilon$ using the “hepthesis” class [14].

Bibliography

- [1] M. A. Thomson. Particle Flow Calorimetry and the PandoraPFA Algorithm. *Nucl. Instrum. Meth.*, A611:25–40, 2009.
- [2] J. S. Marshall, A. Mäijnnich, and M. A. Thomson. Performance of Particle Flow Calorimetry at CLIC. *Nucl. Instrum. Meth.*, A700:153–162, 2013.
- [3] Halina Abramowicz et al. The International Linear Collider Technical Design Report - Volume 4: Detectors. 2013.
- [4] Toshinori Abe et al. The International Large Detector: Letter of Intent. 2010.
- [5] Toshinori Abe et al. The International Large Detector: Letter of Intent. 2010.
- [6] Serguei Chatrchyan et al. Energy Calibration and Resolution of the CMS Electromagnetic Calorimeter in pp Collisions at $\sqrt{s} = 7$ TeV. *JINST*, 8:P09009, 2013. [JINST8,9009(2013)].
- [7] M. Aharrouche et al. Energy linearity and resolution of the ATLAS electromagnetic barrel calorimeter in an electron test-beam. *Nucl. Instrum. Meth.*, A568:601–623, 2006.
- [8] Pascal Perret. First Years of Running for the LHCb Calorimeter System. *PoS, TIPP2014:030*, 2014.
- [9] Howard S. Budd. CMS central hadron calorimeter. *Nucl. Phys. Proc. Suppl.*, 54B:191–197, 1997. [,191(2001)].
- [10] A. Airapetian et al. ATLAS calorimeter performance Technical Design Report. 1996.
- [11] Lucie Linssen, Akiya Miyamoto, Marcel Stanitzki, and Harry Weerts. Physics and Detectors at CLIC: CLIC Conceptual Design Report. 2012.
- [12] B. Pilicer, Helmut Burkhardt, Laurent Gatignon, Andrea Latina, Ercan Pilicer,

Daniel Schulte, Ilhan Tapan, and Rogelio Tomás. Study of Muon Backgrounds in the CLIC Beam Delivery System. In *Proceedings, 6th International Particle Accelerator Conference (IPAC 2015): Richmond, Virginia, USA, May 3-8, 2015*, page TUPTY032, 2015.

- [13] Andr   Sailer. *Radiation and Background Levels in a CLIC Detector due to Beam-Beam Effects*. PhD thesis, CERN, 2012-05-09.
- [14] Andy Buckley. The hepthesis L  T  X class.

List of figures

1.1	A typical simulated 250 GeV jet in the CLIC_ILD detector, with labels identifying constituent particles. Image taken from [2].	3
1.2	(a) Quadrant view of the ILD detector concept. The interaction point is in the lower right corner of the picture. Dimensions are in mm. (b) An artistic view of the ILD detector concept. Figures taken from [3].	4
1.3	Vertex detector design for ILD. Figures taken from [4].	6
1.4	(a) Drawing of the proposed end-plate for the TPC. In the insert a back frame, which is designed to support the readout modules, is shown. (b) Conceptual sketch of the TPC system showing the main parts of the TPC (not to scale). The central electrode generates the axial electric field, the endplates collect the ionisation electrons, the field strips help to maintain a uniform electric field across the TPC and the voltage divider strips maintains the voltage difference between the anode and cathode. The field strips are held at fixed voltages such that they replicate the electric field produced by the electrodes. This reinforcing of the electric field configuration minimises non-uniformities in the electric field. The field cage of the TPC is not shown.	7
1.5	(a) A 3D detailed GEANT4 simulation description of the silicon system. (b) A quadrant view of the ILD silicon envelope made of the four components SIT, SET, ETD and FTD as included in the full MOKKA simulation. Figures taken from [3].	8

1.6	A half-disk for the FTD showing the petal concept. The rightmost zoom image shows a detail of the end-of-petal area that houses the read-out electronics. The leftmost image shows the region at $R = 8$ cm where both the column width and the R -dimension of the pixels changes. Figures taken from [3].	9
1.7	Cross section through ECal layer for (a) silicon and (b) scintillator option. Figures taken from [3].	11
1.8	The sensitive layers of the ILD muon system. Figure taken from [3]. . .	13
1.9	The very forward region of the ILD detector. LumiCal, BeamCal and LHCAL are carried by the support tube for the final focusing quadrupole, QD0, and the beam pipe. Figure taken from [3].	14
1.10	(a) Longitudinal (top quadrant) and (b) transverse cross section of the CLIC_ILD detector. Figures taken from [11].	16
1.12	Schematic showing the definition of the pseudo-layer assignment for calorimeter hits. The solid lines indicate the positions of the physics ECal layers and the dashed lines show the definition of the virtual pseudo-layers. (a) The xy -view showing the ILD ECal stave structure. (b) The xz view showing a possible layout for the ECal barrel/endcap overlap region. The pseudo-layers are defined using projection back to the IP. Figures taken from [1].	22
1.13	The main topological rules for cluster merging: (a) looping track segments; (b) track segments with gaps; (c) track segments pointing to hadronic showers; (d) track-like neutral clusters pointing back to a hadronic shower; (e) back-scattered tracks from hadronic showers; (f) neutral clusters which are close to a charged cluster; (g) a neutral cluster near a charged cluster; (h) cone association; and (i) recover of photons which overlap with a track segment. In each case the arrow indicates the track, the filled points represent the hits in the associated cluster and the open points represent hits in the neutral cluster. Figures taken from [1].	23

List of tables

1.1	The approximate jet fractions and energy resolutions for charged particles (X^\pm) of energy E_{X^\pm} , photons (γ) of energy E_γ and neutral hadrons (X^0) of energy E_{X^0} . Taken from [1].	2
1.2	Coverage of the supplementary silicon tracking systems in the ILD detector. In this table θ is the polar angle with respect to the beam direction. Taken from [3].	8
1.3	Comparison of the nuclear interaction length λ_I , radiation length X_0 and Molière radius for iron, copper, tungsten and lead. Table taken from [1].	10
1.4	Comparison of the ECal energy resolutions for various experiments. .	11
1.5	Comparison of the HCal energy resolutions for various experiments. .	12